Electromagnetic–Thermal Analyses of Distributed Antennas Embedded Into a Load-Bearing Wall

Lauri Vähä-Savo, *Graduate Student Member, IEEE*, Katsuyuki Haneda, *Member, IEEE*, Clemens Icheln, and Xiaoshu Lü

***Abstract*— The importance of indoor mobile connectivity has increased during the last years, especially during the Covid-19 pandemic. In contrast, new energy-efficient buildings contain structures like low-emissive windows and multilayered thermal insulations which all block radio signals effectively. To solve this problem with indoor connectivity, we study passive antenna systems embedded in walls of low-energy buildings. We provide analytical models of a load-bearing wall along with numerical and empirical evaluations of wideband back-to-back spiral antenna system in terms of electromagnetic- and thermal insulation. The antenna systems are optimized to operate well when embedded into load-bearing walls. Unit cell models of the antenna-embedded load-bearing wall, which are called *signal-transmissive walls* in this article, are developed to analyze their electromagnetic and thermal insulation properties. We show that our signal-transmissive wall improves the electromagnetic transmission compared to a raw load-bearing wall over a wide bandwidth of 2.6–8 GHz, covering most of the cellular new radio (NR) frequency range 1 (FR1), without compromising the thermal insulation capability of the wall demanded by the building regulation. Optimized antenna deployment is shown with 22 dB improvement in electromagnetic transmission through the load-bearing wall.**

***Index Terms*— Antenna systems, energy-efficient buildings, outdoor-to-indoor (O2I) communication, radio transparency, thermal transmittance.**

I. Introduction

THE fifth-generation cellular networks, which have been rolled out during the last couple of years, promise higher data rates compared to legacy systems. With new radio (NR) frequency range 1 (FR1), where the frequencies are below 6 GHz, the capacity can be increased up to 20 times higher than the fourth-generation systems [1]. At the same time providing sufficient indoor coverage has become more challenging [2]. During the Covid-19 pandemic, the use of mobile internet has risen drastically all over Europe [3] and in the world. The problems with indoor coverage become increasingly serious in energy-efficient buildings. They have e.g., multilayered thermal insulating layers, low-emission airtight windows, and other signal barriers which all make the outdoor-to-indoor (O2I) communication challenging, if not impossible [4], [5]. This trend will be strengthened as international building regulations like [6] have been taken into national regulation. The goal of the regulation is to move toward zero-energy buildings which makes the cellular coverage by outdoor base stations even more challenging.

To improve indoor coverage, both active and passive solutions have been studied in recent years. Active solutions include indoor base stations [7], [8] and repeaters [9], [10], [11]. The problem with the active solutions is that those often need a radio frequency (RF)-over-fiber network. These are expensive systems and need additional energy to operate. The passive solutions are often e.g., low-emissivity windows with frequency-selective surfaces [12] or signal slots [13], [14]. The passive solution does not need extra energy to operate, but the problem is often that those have relatively narrow passbands in the RF. In addition, at least to our best knowledge, there is no commonly used passive solution that could operate over the whole lifespan of the building.

In this article, we improve the work of our own [15] and present a numerical and empirical evaluation of passive antenna systems embedded into a building wall called the *signal-transmissive wall*. The main purpose of the embedded antenna system is to create a pathway for the RF signals to propagate into a low-energy building with lower penetration losses. This concept was introduced with an antenna system at a point frequency in [15], but in this article, we introduce a wideband spiral antenna system that significantly reduces the penetration loss compared to load-bearing wall. The antenna system is also designed to keep the thermal insulation of the wall to the level stated by the nation-building code of Finland [16]. In this article, we show first time the optimized deployment of an ordinal antenna system on a wall through multiphysics criterion.

In summary, the novel contributions of the present article are summarized as the following threefold.

1) We developed a wideband back-to-back spiral antenna system embedded onto the wall, leading to a signal-transmissive wall operating over a large portion of NR FR1 band i.e., between 2.6 and 8 GHz.

Manuscript received 13 February 2023; revised 10 May 2023; accepted 24 May 2023. Date of publication 13 June 2023; date of current version 4 August 2023. This work was supported by the Academy of Finland Research Project "Signal-Transmissive-Walls with Embedded Passive Antennas for Radio-Connected Low-Energy Urban Buildings (STARCLUB)," decision under Grant 323896. *(Corresponding author: Lauri Vähä-Savo.)*

Lauri Vähä-Savo, Katsuyuki Haneda, and Clemens Icheln are with the Department of Electronics and Nanoengineering, Aalto University School of Electrical Engineering, FI-00076 Espoo, Finland (e-mail: lauri.vaha-savo@aalto.fi).

Xiaoshu Lü is with the School of Technology and Innovations, University of Vaasa, 65200 Vaasa, Finland.

Color versions of one or more figures in this article are available at https://doi.org/10.1109/TAP.2023.3284368.

Digital Object Identifier 10.1109/TAP.2023.3284368

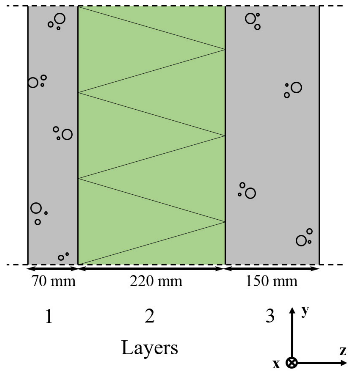

Fig. 1. Concrete sandwich panel for load-bearing wall. The panel is made of 70 mm-thick reinforced concrete (layer 1), 220 mm-thick rock wool for thermal insulation (layer 2), and 150 mm-thick reinforced concrete for structural bearing (layer 3).

2) We perform an analytical, numerical, and empirical evaluation of the electromagnetic- and thermal insulation of the wall to evaluate the efficacy of the signal-transmissive wall; and finally.
3) We perform a numerical study showing the effect of antenna system installation on the reduction of electromagnetic transmission losses and maintained thermal insulation.

The rest of the article is organized as follows. Section II defines the load-bearing wall of modern buildings and analytical expressions of electromagnetic and thermal properties of the wall. Section III introduces the design of a spiral antenna system embedded into the load-bearing wall, along with experimental verification of the spiral antenna design in free space. Section IV shows a comparison of electromagnetic and thermal transmission between the bare load-bearing wall and the signal-transmissive wall. The electromagnetic properties of the designed signal-transmissive wall are verified experimentally. After that, the optimized installation of the antenna systems is numerically evaluated through an electromagnetic–thermal criterion. Section V concludes the work and gives some insights for future works.

II. Electromagnetic and Thermal Insulation of a Load-Bearing Wall

A general structure of a bare load-bearing wall that we study as an example in this article is illustrated in Fig. 1. The wall is made from 220 mm thick rock wool layer for thermal insulation, which is sandwiched between 70 and 150 mm thick concrete layers. A concrete wall can be reinforced by adding a rebar net. Effects of this net are slightly increased penetration losses and cut-off frequency that appears typically below 1 GHz RF. The net does not impact the thermal insulation either, so we do not consider them in this study. The following summarizes analytical models of the electromagnetic and thermal transmission properties of the wall, along with its comparison with numerical simulations to cross-validate the two approaches. This validation shows that our numerical method is in line with the theory and hence has the fidelity needed to perform the analysis in this work. It is important to remember that the goal of this work is to improve electromagnetic transmission and at the same time maintain thermal insulation so both analyses are crucial for the success of this study.

TABLE I

Dimensional and Electrical Properties of the Load-Bearing Wall

Layer # / Material	Thickness [mm]	Relative permittivity model ϵ_r in (1) [17]
#1 Concrete	70	$a = 5.24$, $b = 0$, $c = 4.6 \times 10^{-2}$, $d = 0.7822$
#2 Rock wool	220	$a = 1.48$, $b = 0$, $c = 1.1 \times 10^{-3}$, $d = 1.0750$
#3 Concrete	150	$a = 5.24$, $b = 0$, $c = 4.6 \times 10^{-2}$, $d = 0.7822$

A. Electromagnetic Insulation of the Wall

1) Analytical Model: The electrical parameters of concrete and rock wool are defined from 1 to 100 GHz in ITU-R P.2040 [17]. The relative permittivities of different building materials are defined as [17]

$$\epsilon_r(f) = \epsilon' - j\epsilon'' = af^b - j\frac{cf^d}{\epsilon_0\omega} \quad (1)$$

where the a, b, c, and d are summarized in Table I that determine the frequency-dependent permittivity while f is the RF in GHz. We model the wall as a three-layered dielectric structure that is infinitely long in x and y directions as defined by the coordinate system in Fig. 1. The calculation model for the reflection and transmission coefficient of a planar dielectric slab with N-layered is also defined in [17] and can be used to calculate the electromagnetic transmission through the bare load-bearing wall.

2) Numerical Study: Electromagnetic insulation of the load-bearing wall was numerically simulated using the *CST Studio Suite*.[1] An infinitesimally large load-bearing wall is considered along with a plane electromagnetic wave incidence. The infinitely large wall can be simulated using unit cell boundary conditions with two Floquet ports [18] which are placed a quarter wavelength distance away from the outdoor- and indoor-facing sides of the wall which is calculated from the smallest frequency in the simulation. Thereby the small unit cell is copied around itself in $\pm x$ and $\pm y$ directions, making it virtually infinitely large. This means that if an antenna system is placed on a unit cell, it is repeated with the rest of the unit cell and antenna separation will be the same as the x and y dimensions of the unit cell.

We assume a right-handed circularly polarized incoming plane wave. Since the unit cell is larger than the wavelength, the higher order modes must be considered on the receiving side to ensure that all the power coming from the wall is captured. In the simulations, the entire RF band of interests is split into 1 GHz sub-bands to ensure the feasible simulation time. More modes need to be considered on the receiving side at the higher RF. In this study, the number of Floquet modes $N_F = 50 - 100$ is enough to model all the power leaving the wall. The total transmission of the electromagnetic fields through the wall can be calculated by integrating all

[1] https://www.3ds.com/products-services/simulia/products/cst-studio-suite/

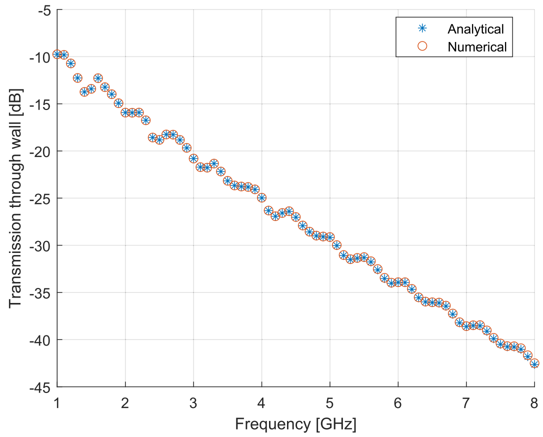

Fig. 2. Electromagnetic transmission through a bare load-bearing wall, comparison between analytical calculation and numerical simulation.

the mode coefficients in the receiving port as $T = \sqrt{\sum |T_i|^2}$, $i = 1, \ldots, N_F$, given by numerical simulations in the CST Studio.

The transmission coefficients of the bare load-bearing wall derived from the analytical model and numerical simulations are compared to cross-validate both approaches. As we see from Fig. 2, the electromagnetic transmission coefficients from the two approaches agree perfectly.

B. Thermal Insulation of the Wall

1) Analytical Study: Thermal insulation of the wall is often described by conductive heat flux. In the case of steady state, the heat flux density can be evaluated using a sample wall, whose dimensions in x and y directions are much larger than in the z direction, so that 1-D steady-state heat conduction can be assumed. The heat flux depends on the types of materials and the number of wall layers as well as the temperature difference between different sides of the wall sample. Therefore, we use a heat transfer rate per temperature, also called a *U-value* and *thermal transmittance*, as an evaluation metric. Walls with smaller U-values are preferred for energy-efficient buildings. The thermal transmittance is defined as the inverse of the thermal resistance as

$$U = \frac{1}{R_{\text{tot}}} = \frac{1}{R_{\text{si}} + R_{\text{n}} + R_{\text{se}}} \tag{2}$$

where R_{si} and R_{se} are indoor-facing and outdoor-facing thermal surface resistances. The thermal resistance of a wall is affected by radiation from heat sources influencing the wall, e.g., the sun and electrical equipment. Also, air convection affects the thermal surface resistances on both indoor- and outdoor-facing sides of the wall. The ISO6946 standard [19] for building components and elements recommends that evaluation of thermal transmittance of walls is made with $R_{\text{si}} = 0.13$ and $R_{\text{se}} = 0.04$ m$^2 \cdot$ K/W. Thermal resistance R_{n} of the multilayered wall can analytically be derived for a simple wall made of layers of N slabs by

$$R_{\text{n}} = \sum_{n=1}^{N} \frac{d_n}{\lambda_n} \tag{3}$$

TABLE II
THERMAL CONDUCTIVITIES OF MATERIALS USED IN EMBEDDED ANTENNA SYSTEM

Material	Thermal conductivity at 20°C λ [W/(m · K)]
Rogers RT/duroid 5880	0.2
Styrofoam (EPS)	5×10^{-2}
Stainless steel	15
Copper	400
Teflon (PTFE)	0.24
Rockwool	3.5×10^{-2}

where d_n is the thickness of layer n and λ_n is a thermal conductivity [W/(m · K)] of layer n.[2]

2) Numerical Study: To simulate the thermal transmittance of the wall, *Comsol Multiphysics heat transfer module*[3] was used. The same unit cell model was used as in the electromagnetic simulations. The values of thermal conductivity can be found in Table II for each layer of the bare load-bearing wall shown in Fig. 1. Convective heat fluxes $q_{\text{si}} = T_{\text{si}}/R_{\text{si}}$ and $q_{\text{se}} = T_{\text{se}}/R_{\text{se}}$ as a boundary condition were assigned for indoor- and outdoor-facing sides of the wall, where $T_{\text{si}} = 293$ K and $T_{\text{se}} = 271$ K are the indoor- and outdoor-facing surface temperature, respectively. These convective heat fluxes work as a source of our thermal simulation. For the four sides of the unit cell facing toward $\pm x$- and $\pm y$-directions in Fig. 1 thermal insulation boundaries were assigned so that the wall was virtually infinitely large along with those directions. The thermal insulation boundary ensures that the normal component of conductive heat flux on the boundary is zero, i.e., no heat is dissipating on those four sides. To verify the simulation model, we compared the simulated thermal transmittance to the analytically calculated one. For the comparison, we used thermal conductivity of 1.3 W/(m · K) which corresponds to a medium-density concrete [20]. Both simulation and analytical calculation give thermal transmittance of 0.15 W/(m^2 · K) validating our model.

III. ANTENNA SYSTEM

A. Design of a Spiral Antenna System

Our antenna system contains two antenna elements located on different sides of the wall connected back-to-back with coaxial cables, similar to our earlier work [15]. However, the earlier work uses patch antennas that cover only 1.3% of the relative bandwidth. Wideband antennas are preferable over narrow ones since those can cover a wide variety of cellular services. The antenna system embedded into the load-bearing wall is shown in Fig. 3 where the Archimedean spiral antennas are designed and installed instead of the patch antennas. We chose the spiral antenna because of its compact size. Compared to e.g., bowtie antenna, the size of the spiral antenna is roughly half which makes it possible

[2] A symbol for thermal conductivity λ should not be confused with the wavelength of electromagnetic waves in this article. We follow the notation of ISO6046 [19] for the symbol λ.

[3] www.comsol.com

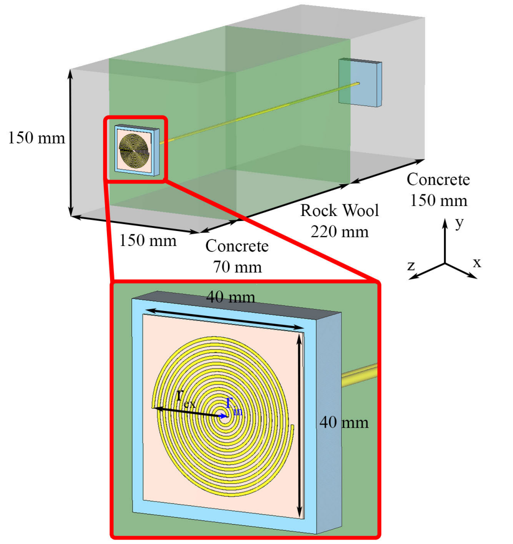

Fig. 3. Unit cell of load-bearing wall with embedded back-to-back spiral antenna system.

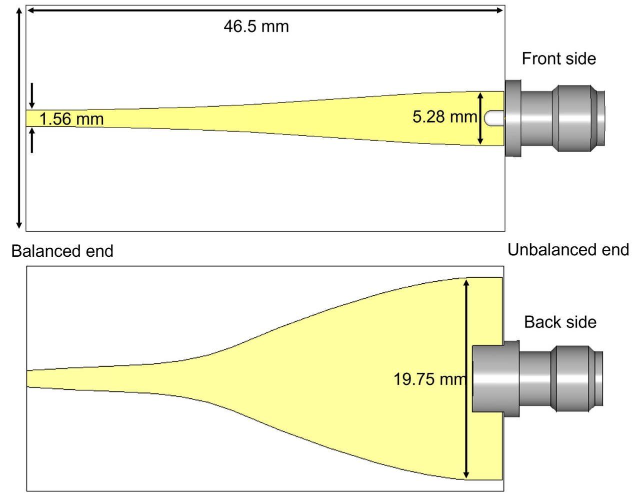

Fig. 4. Front and back view of experimentally tapered microstrip balun. Supporting legs on the top side of the connector are removed to ensure that the connector does not touch the feed line of the balun.

to embed them in the wall densely. As the spiral antennas are electrically balanced, a dual-coaxial cable is introduced to connect two antennas on different sides of the wall. The outer conductors of two coaxial cables are galvanically connected, making them a balanced line with double the characteristic impedance of the original coaxial cable. This way a similar characteristic impedance is realized for the spiral antennas and the dual-coaxial cable, thereby omitting the need for a matching network or balun. Each coaxial cable has a center pin with 0.287 mm diameter and an outer connector with 1.76 mm diameter and 0.2 mm thickness. Low-density Teflon (PTFE) with a dielectric constant of 1.75 and $\tan\delta = 0.004$ is used as an insulating layer of cables. A single and dual-coaxial cable, therefore, shows 82 and 164 Ω characteristic impedance. As reported in [15], the thermal transmittance of the wall is too high if copper coaxial cables are going through the whole wall. The thermal conductivity of stainless steel is about 27 times smaller than copper, as shown in Table II. This makes it a suitable conductor material for coaxial cables going through the wall. According to CST simulations, a coaxial cable loss is 3.7 and 6.3 dB at 3.5 and 8 GHz respectively, while the loss of bare load-bearing wall is 23.2 and 42.5 dB at 3.5 and 8 GHz, showing much greater losses of wave propagation through the wall compared to the coax cable of the same length. The performance of our solution is not significantly affected even by doubling the thickness of the insulating layer inside the wall. Because the thermal conductivity of stainless is low, the cables cannot be soldered together so we decided to place them inside heat shrink tubing. The 3-D model of the unit cell of the antenna system embedded into the wall can be downloaded from [21].

B. Spiral Antenna Element and Its Measurements in Free Space

The spiral antenna is realized on top of 0.5 mm thick Rogers RT/duroid 5880 laminate ($\epsilon_r = 2.2$, $\tan\delta = 9.0 \times 10^{-4}$) with the size of 40 × 40 mm. The legs of the spiral are realized with lines of 0.68 mm width. The number of turns in the spiral is 6 with the internal and external radius of $r_{in} = 1.08$ mm and $r_{ex} = 17.4$ mm. Since the internal radius is the same as the radius of our coaxial cable, each leg of the spiral antenna can be connected to the center pins of the dual-coaxial cable to build the back-to-back antenna systems.

To be able to test the spiral antenna in free space, without the influence of a wall, a balancing unit (balun) is needed. An experimentally tapered balun, similar to the one in [22], was designed. The balun is realized on top of 1.575 mm thick Rogers RT/duroid 5880 laminate with the size of 22 × 46.5 mm. The unbalanced end of the balun is a transmission line with 5.28 mm width to have 50 Ω input impedance. The tapering of the line and the ground plane leads to a parallel plate line of 1.56 mm width so that the input impedance at the balanced end is 164 Ω which is similar to the input impedance of the spiral antenna and the dual-coaxial cable. The ground plane printed on the backside of the balun is 19.75 mm wide on the unbalanced end and is tapered to the same width as the feed line. The top and bottom sides of the balun are shown in Fig. 4.

Two vias were used to connect each leg of the spiral antenna and the balun. Via dimensions are similar to the center connectors of the dual-coaxial cable to ensure a similar current transition with balun and dual-coaxial cable. Amphenol SV Microwave 2.92 mm connector (Mfr. No: 1521-60051) was used to connect the antenna to the VNA. To make sure that the connector does not touch the feed line, supporting legs on the top side of the connector are removed, as can be seen from Fig. 4. Fig. 5 shows the measured and simulated reflection coefficients of the balun attached to the spiral antenna between 2 and 8 GHz covering most of the NR FR1. The analysis is limited below 8 GHz since we do not have a powerful computational capability enough to simulate the infinitely large antenna-embedded wall above 8 GHz. The measured reflection coefficient is smaller than the simulated ones over

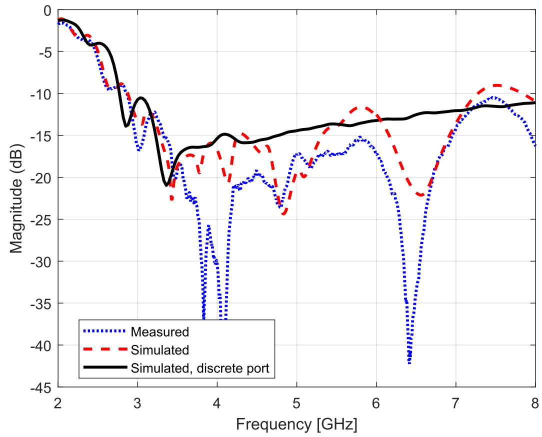

Fig. 5. Reflection coefficient of the spiral antenna in free space, measured with the balun.

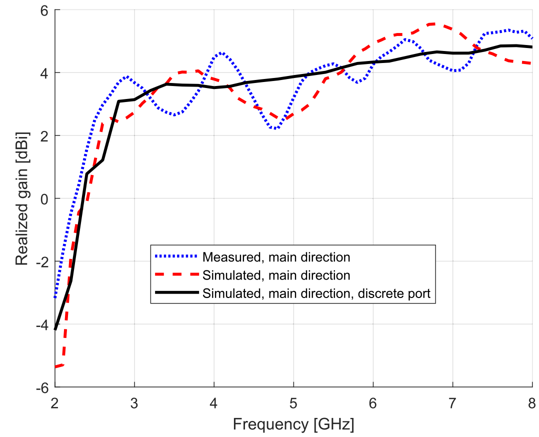

Fig. 6. Realized gain of the spiral antenna with the balun in free space.

most of the frequency band. This could be caused by the manufacturing tolerances since the balun is experimentally tapered and small changes in balun dimensions can improve the balun. Both simulated and measured curves show ripples over the frequency band. This is most likely caused by imperfect connector and soldering which can cause small changes to the matching level over the frequency range. Also, the matching between the antenna and balun can vary a little over the frequency. The black line corresponds to the simulation with a discrete port with 164 Ω normalization impedance, i.e., that of the dual-coaxial cable. All simulated and measured reflection coefficients agree well with each other.

The realized gain of the spiral antenna was measured in an anechoic chamber between 2 and 8 GHz. Fig. 6 shows the maximum of realized gain of the spiral antenna over the frequency to broadside direction $+z$. The simulation with a discrete port has a much smoother gain pattern over the frequency, suggesting that the balun causes some losses and standing waves to the system. The standing waves can be caused by e.g., imperfect matching between the antenna, balun, and VNA. Although the measured maximum gain fluctuates more than the simulated one, the overall trend of the realized gains agrees with each other, confirming the efficacy of the designed spiral antenna.

IV. Antenna-Embedded Wall

A. Embedding Antenna Systems on the Wall

The spiral antenna cannot be placed directly on the top of concrete because concrete causes detuning and losses to the antenna. At the same time, in free space, a spiral antenna radiates the same way in $\pm z$ directions on Fig. 3. To improve the radiation efficiency of the antenna and direct more power to the $+z$-direction defined in Fig. 3, the antenna is backed with the Rohacell foam when integrated with a wall. The foam is placed inside of the concrete layer to create a small air gap between the antenna and the concrete hence maintaining the high radiation efficiency of the antenna over the frequency. The purpose of the foam layer is to decouple the high permittivity concrete from the antenna. As the effective permittivity of the

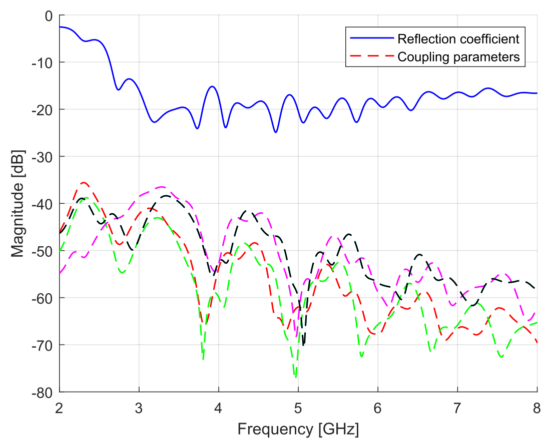

Fig. 7. Reflection coefficient and coupling parameters of spiral antenna element on top of a concrete slab.

antenna with foam layer is closer to one on free space, the antenna operates similarly on top of concrete as in free space. The thickness of the foam was optimized in simulations to maximize the radiation efficiency when the spiral antenna was placed on top of a 150 × 150 × 50 mm^3 concrete slab. The antenna element was backed with a block of foam with the size of 50 × 50 mm^2. The thickness was varied from 0 to 10 mm. The antenna was fed by the dual-coaxial cable described in Section III-A. The radiation efficiency increases monotonically when the foam layer is thicker. Without the foam layer, the average radiation efficiency of the antenna between 2.5 and 8 GHz is −12 dB and a mean realized gain of −6.4 dBi toward $+z$-direction. When we add 10 mm thick foam to the backside of the antenna the average radiation efficiency is −3.1 dB and the mean realized gain of 4.6 dBi, thereby choosing 10 mm thick Rohacell in our back-to-back antenna system. Because of the limited capability to feed differential signals with our measurement equipment, we cannot verify these results with measurements.

Fig. 7 shows the reflection coefficient and mutual coupling of the spiral antenna element on top of a concrete slab. The reflection coefficient is below −10 dB when the frequency is higher than 2.64 GHz. Mutual coupling between adjacent antennas is less than −36 dB over the whole frequency band

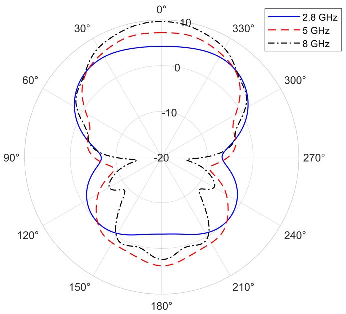

(a)

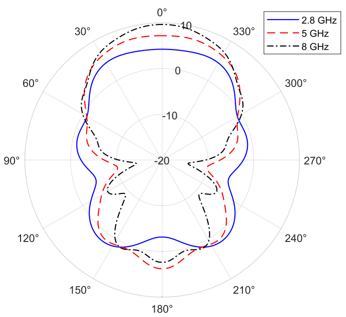

(b)

Fig. 8. Radiation pattern of spiral antenna element on top of concrete slab (a) $\phi = 0°$ and (b) $\phi = 90°$.

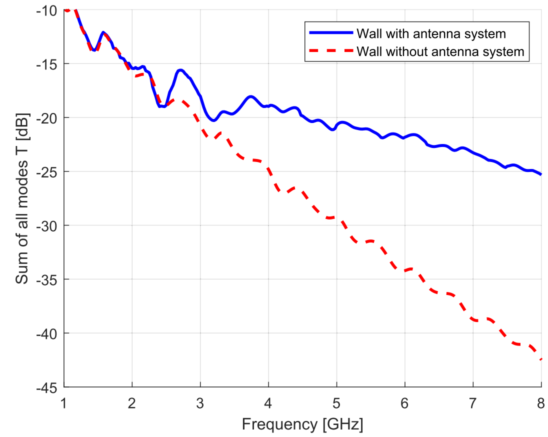

Fig. 9. Simulated transmission through the infinitely large load-bearing wall with and without the embedded spiral antenna system. The unit cell sizes in x and y directions are all 150 mm.

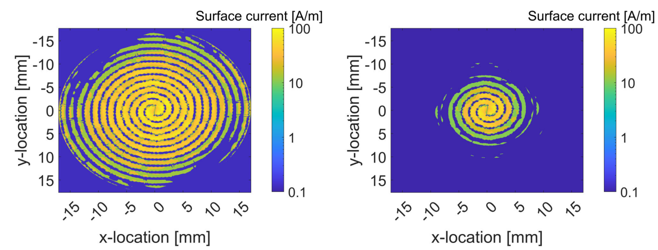

(a) (b)

Fig. 10. Surface current of the spiral antenna at (a) 3 GHz and (b) 8 GHz.

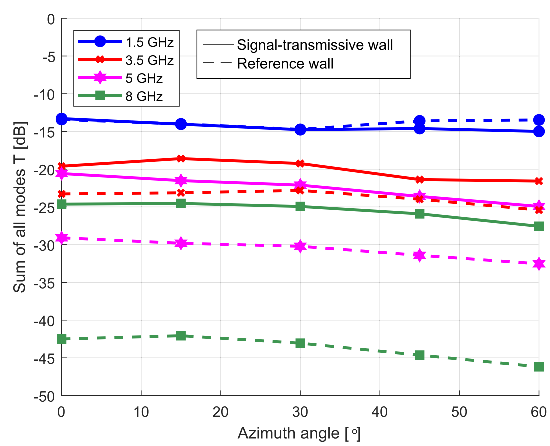

Fig. 11. Simulated transmission through the infinitely large load-bearing wall with and without the embedded spiral antenna system with a changing incident azimuth angle of a plane wave from 0° to 60° T°. The unit cell size spans 150 mm in x and y directions.

meaning that individual elements do not couple to each other. Fig. 8 shows the radiation pattern of one antenna element at 2.8, 5, and 8 GHz on top of a concrete slab. Similarly, as in the case of free space, the maximum gain of the spiral antenna element increases with the frequency. The noticeable difference is that the radiation pattern is not symmetric but the radiation toward the back direction is smaller than the main direction. The maximum realized gain is increased from 4.2 up to 9.6 dBi which is more than the rice in free space. This can be explained by the concrete slab reflecting some radiation. The operation of the antenna element on top of the concrete is tested by measuring the antenna system embedded into a wall.

B. Electromagnetic Transmission of the Infinitely Large Antenna-Embedded Wall

The total electromagnetic transmission of the wall was simulated with and without an antenna system as explained in Section II. Fig. 9 shows the transmission coefficient from 1 to 8 GHz. The unit cell size is 150×150 mm^2. It is important to remember that the unit cell dimensions in x and y directions are the same as the antenna separations on the infinitely large wall. We used a right-handed circular polarized incident plane wave. As can be seen from the Figure, the antenna system starts to improve the transmission around 2.6 GHz and above. The transmission coefficients decrease as the frequency increases even after embedding the antenna systems. This is due to the increasing cable loss and also decreasing effective aperture size of the spiral antenna. A decrease in the effective aperture can be observed from the simulated surface current plot at 3 and 8 GHz depicted in Fig. 10 at 8 GHz currents flow in roughly five times smaller area than at 3 GHz. Up to 17 dB improvement of the transmission coefficient was observed at 8 GHz by embedding the antenna systems to the wall. Compared to our previous work, the bandwidth of the antenna system is improved from 1.3% to 3.1:1. At the same time, both antenna systems realize a similar improvement of the transmission coefficient at 3.5 GHz.

Next, the effect of azimuth incident angle is studied at 1.5, 3.5, 5, and 8 GHz. For this study, we need to increase the number of simulated Floquet modes because of the increased incident angle. Also, scattering caused by antennas and cables will increase the number of propagating modes through the

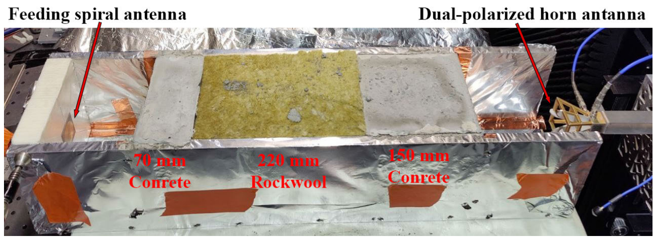

Fig. 12. Measurement setup for the electromagnetic transmission measurements. The left side is the feeding spiral antenna and on the right side, the dual-polarized horn antenna. The top-side metal is removed for the picture.

wall. Fig. 11 shows the transmission coefficient in the case of 15°, 30°, 45°, and 60° incident angles. The figure shows that transmission through the wall with and without the antenna system is decreasing when the azimuth incident angle is increased. This is expected since we know from [17] that the reflection coefficient of concrete is increasing when the incident angle is greater. Also, the gain of the spiral antenna is decreasing with greater incident angles. The antenna system clearly improves the transmission through the wall even with the glazing incident angle. For example, at 8 GHz with 60° incident angle, the improvement is 18.6 dB which is 1.6 dB more than in the case of a normal incident. Measuring these results would demand us to manufacture a large signal-transmissive wall which is not possible in our laboratory. Instead of using multiple incident angles in the measurements, we concentrate on showing the signal-transmissive wall's efficacy in the case of a normal incident.

C. Manufactured Wall Samples

As it is not possible to manufacture infinitely large wall as was performed in the simulations, wall samples of 150 × 150 mm^2 unit cell size were manufactured for our measurements. These small samples are enclosed in metallic waveguides for electromagnetic measurements. The waveguides are used *only* for the purpose of comparing the simulated and measured antenna-embedded walls to verify its whole design. If the measurements agree with simulations when the antenna-embedded wall is enclosed by the metallic waveguide, the same should apply to other setups of the antenna-embedded walls. The wall samples are cast inside the waveguides to ensure that the samples are as close to the sizes of the waveguides as possible. The waveguide-enclosed antenna-embedded wall being the device-under-test, the same spiral antenna with the balun that we used in free space measurements was used as a feed antenna. As a receiving antenna, we use a dual-polarized double-ridge horn antenna. The setup using the waveguide allows for measuring all the energy that is transmitted through the wall sample. The same setup was built in a simulation for comparison with measurements, where a waveguide port with a large enough amount of modes is used as a receiving antenna to ensure that all the transmitted power is detected.

The load-bearing wall consists of a rockwool layer in addition to concrete. To ensure the correct thermal behavior of the wall, the Paroc COS 5ggt rockwool was used, which

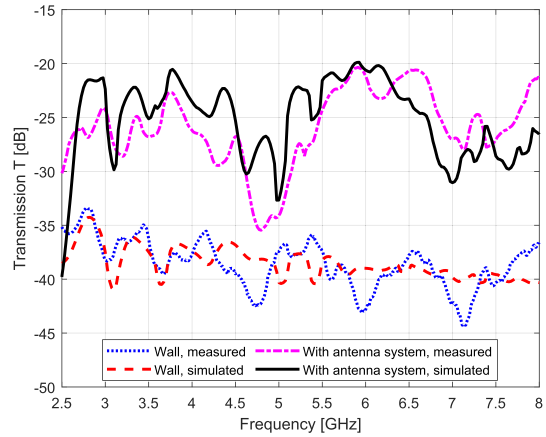

Fig. 13. Measured and simulated total electromagnetic transmission through the wall sample inside the waveguide.

is widely used in concrete sandwich elements in Finland. The antenna system and rockwool were placed inside the waveguide and the concrete was cast in. Also, a wall without the antenna system was cast as a reference sample. The waveguide has 150 mm extra length at both ends of the wall sample, leading to the total length of the waveguides being 740 mm. The empty space created by the extra length of the waveguide is needed for placing the transmitting and receiving antennas. The curing time of concrete varies based on the temperature and humidity of the casting site. Concrete reaches its final strength roughly in 28 days [23] so any measurements were performed after that period.

D. Electromagnetic Insulation of the Antenna-Embedded Wall Inside a Waveguide

Prior to electromagnetic measurements of the antenna-embedded wall, a transmission coefficient of *only* the casted concrete block in the waveguide was measured to estimate the complex permittivity of the concrete. It turned out that the casted concrete had a moisture content that led to higher permittivity than the one in the ITU model. The permittivity was estimated by solving the analytical model of transmission coefficients for a slab shown in ITU-R p.2040 [17]. The estimated parameters for concrete to be used in (1) are $a = 5.84$, $b = 0$, $c = 0.205$, and $d = 0.06$. We use this measured permittivity to compare the transmission through the reference and antenna-embedded walls between the measurements and the simulations.

Fig. 12 shows the measurement setup used in the electromagnetic transmission measurements without the top-side waveguide wall. The feeding spiral antenna is mounted at the center of a piece of Styrofoam. The corners of the waveguide are strengthened with copper tape. During the measurements, the top side of the waveguide wall is also used. Fig. 13 shows the total transmission through the wall with and without the spiral antenna system. The losses caused by the measurement system, including the waveguide, are calibrated by normalizing the wall measurement coefficients with those with an empty waveguide of the same dimension. The measured and simulated transmission agrees well with each other. The improvement due to the inclusion of antenna systems is on average 16 dB between 2.5 and 8 GHz. The two dips in the transmission around 4.8 and 7.3 GHz are caused by feed antenna coupling to the embedded antenna system. These dips would be smaller if the distance between the feed antenna and the embedded antenna would be larger. All the curves fluctuate more than the ones shown in Fig. 9. This is caused by the increased moisture in the samples. The measured transmissions also fluctuate more than simulations which can be explained by the heterogeneity of the measured concrete, where the simulated concrete is homogeneous. The impact of the antenna system in improving electromagnetic transmission through the load-bearing wall is clear.

E. Thermal Insulation of the Antenna-Embedded Wall

The thermal conductivities of most materials used in the signal-transmissive wall are given by manufacturers as listed in Table II. But the concrete was mixed in our lab and its thermal properties are unknown. ISO10456 [20] gives nominal thermal properties of most used construction materials. A sample of our concrete was measured with *C-Therm TCI thermal conductivity measurement system*[4] to characterize the thermal conductivity of our concrete. C-Therm TCI is based on a modified transient plane source technique, requiring only one probe. A single measurement of thermal conductivity takes only a few seconds. The measurement was repeated a few times to make sure that the results are repeatable. The thermal conductivity estimate of our concrete was 1.3 $\mathrm{W/(m \cdot K)}$ which is similar to medium density concrete in [20]. The measured thermal conductivity of concrete is used for the following thermal simulations.

The thermal insulation of the wall was numerically simulated with the same structures as the electromagnetic unit cell simulations using the method described in Section II. The wall without the antenna system has a U-value of 0.15 $\mathrm{W/(m^2 \cdot K)}$, while that of the antenna-embedded wall is 0.16 $\mathrm{W/(m^2 \cdot K)}$, showing a slight increase. The present U-value of the antenna-embedded wall is better than the one in our previous work [15], where we reported a U-value of 0.51 $\mathrm{W/(m^2 \cdot K)}$, most likely because the stainless steel conductor was used in coaxial cables instead of copper. Also, the reduced size of the cables decreases the U-value. The presented antenna-embedded wall has a lower U-value than 0.17 $\mathrm{W/(m^2 \cdot K)}$ limit given in the national building regulation [16].

F. Impacts of Antenna System Separation on Electromagnetic and Thermal Insulation

Now that the analysis methods of the signal-transmissive wall are verified through experiments, we are ready to study the effect of antenna separation on electromagnetic transmission and thermal transmittance. When antenna systems are placed more densely on the wall the U-value will increase. The national building code of Finland says that the U-value of the wall cannot be higher than 0.17 $\mathrm{W/(m^2 \cdot K)}$ [16], as mentioned in Section IV-E. The antenna separation is first studied in terms of thermal transmittance by changing the squared unit cell size in x and y directions by varying their values from 70 to 200 mm to identify the smallest possible cell size that meets the 0.17 $\mathrm{W/(m^2 \cdot K)}$ limit. Fig. 14 plots the results, showing that 90 mm antenna system separation satisfies the 0.17 $\mathrm{W/(m^2 \cdot K)}$ threshold. The thickness of planar antennas including the metallization is thin leading to very small thermal resistance according to (3). To make numerical simulations faster, we can leave the antenna metallization or even the whole antenna structure away and concentrate only on the coaxial cables in the wall [24].

Next, the electromagnetic transmission through the wall is simulated for varying unit cell dimensions from 90 to 200 mm, similar to thermal simulations. The RF was 1.5, 3.5, 5, and 8 GHz. Fig. 15 shows the results including those of raw load-bearing wall. The transmission coefficient is higher with smaller antenna system separations except at 3.5 GHz where 90 mm antenna separation gives 4 dB lower transmission than 100 mm separation. This can be explained by the fact that antenna elements are coupled to

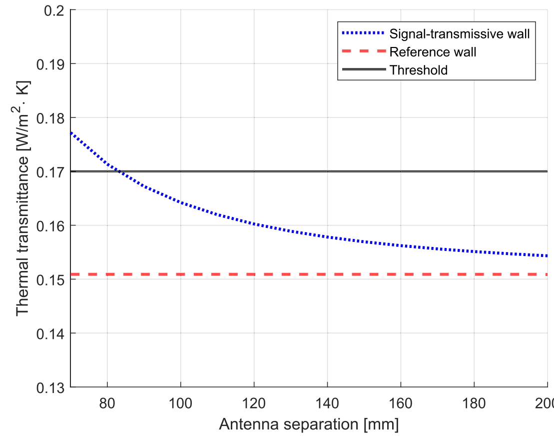

Fig. 14. Simulated thermal transmittance through the infinitely large load-bearing wall with and without the embedded spiral antenna system. The antenna separation varies from 70 to 200 mm.

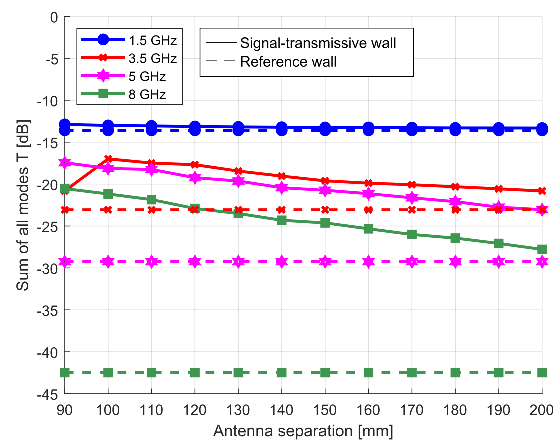

Fig. 15. Simulated transmission through the infinitely large load-bearing wall with and without the embedded spiral antenna system; the antenna system separation varies from 70 to 200 mm.

[4]https://ctherm.com/thermal-conductivity-instruments/tci-thermal-conductivity-analyzer

each other with small separations. For a constant antenna separation, greater effective aperture size leads to stronger coupling as evidenced in Fig. 10. At 8 GHz the transmission is improved by 22 dB with 90 mm antenna separation which is roughly 5 dB more than with the 150 mm separation that was presented in Section IV-B. According to these results, 100 mm antenna system separation gives us the lowest transmission loss through the wall with the current design of the signal-transmissive wall. With 100 mm separation the mutual coupling does not deteriorate the radiation efficiency of the antenna system while the signal-transmissive wall respects the U-value restrictions. It is also good to notice that even with 200 mm antenna system separation the transmission coefficient is improved at all the simulated RF.

V. Concluding Remarks

This article introduces analytical, numerical, and empirical evaluation of the antenna-embedded wall, which is called the signal-transmissive wall. Wideband spiral antenna system was introduced, manufactured and its electromagnetic and thermal transmission characteristics were analyzed. Dual-coaxial cable assembly was introduced to connect two balanced spiral antennas back-to-back without the need for a separate balun or matching network. Penetration loss of load-bearing wall was decreased down to 17 dB at 8 GHz when the antenna system is embedded to the wall every 150 mm, compared to 42.5 dB loss of the bare load-bearing wall. The electromagnetic transmission is improved by more than 6 dB at RF above 4 GHz. The increase of the U-value was so slight that the signal-transmissive wall still achieves the demanded level of national building regulation. The simulated and measured electromagnetic transmissions agree well with each other for the waveguide-enclosed signal-transmissive wall. Antenna systems could be placed as densely as every 100 mm to the load-bearing wall without exceeding the U-value threshold while improving the electromagnetic transmission at 8 GHz by 22 dB. Given the verified improvement of the electromagnetic transmission coefficient through the signal-transmissive wall, its impact on indoor cellular coverage inside low-energy buildings is a subject of further study. These studies include an analytical model that allows us to study in more detail the effects of different components, like antennas and cable assemblies, and the materials used on them on the link budget of radio links involving the embedded antenna systems [24]. We are also doing coverage studies with a ray launcher that allows us to study the effect of the signal-transmissive wall on the O2I channel. How to protect the antenna systems against changing operation conditions needs to be studied in future work to make sure the operation over the lifespan of the building. The signal-transmissive wall should be considered as a possible solution for improving electromagnetic transmission on O2I communication.

References

[1] Nokia. (Nov. 2018). *5G Deployment Below 6 GHz*. [Online]. Available: https://www.rrt.lt/wp-content/uploads/2018/10/Nokia_5G_Deployment_below_6GHz_White_Paper_EN.pdf

[2] Zinwave. (2017). *Cellular in the Workplace Survey, 2017 Connectivity Issues Are Widespread*. [Online]. Available: https://communicationselectronics.com/wp-content/uploads/2021/09/Zinwave-Survey-Report-LP.pdf

[3] R. Wood. (Mar. 2020). *COVID-19: Operators Should be Concerned About the Robustness of Networks Rather Than Capacity*. [Online]. Available: https://www.analysysmason.com/research/content/articles/covid19-robustness-networks-rdnt0/

[4] I. Rodriguez, H. C. Nguyen, N. T. K. Jorgensen, T. B. Sorensen, and P. Mogensen, "Radio propagation into modern buildings: Attenuation measurements in the range from 800 MHz to 18 GHz," in *Proc. IEEE 80th Veh. Technol. Conf. (VTC-Fall)*, Sep. 2014, pp. 1–5.

[5] K. Haneda et al., "5G 3GPP-like channel models for outdoor urban microcellular and macrocellular environments," in *Proc. IEEE 83rd Veh. Technol. Conf.*, May 2016, pp. 1–7.

[6] European Commission. (2019). *European Union Directive on Nearly Zero-Energy Buildings*. [Online]. Available: https://energy.ec.europa.eu/topics/energy-efficiency/energy-efficient-buildings/nearly-zero-energy-buildings_en

[7] S. F. Yunas, "Capacity, energy-efficiency and cost-efficiency aspects of future mobile network deployment solutions," M.S. thesis, Fac. Bus. Technol. Manag., Tampere Univ. Technol., Tampere, Finland, Oct. 2015. [Online]. Available: https://urn.fi/URN:ISBN:978-952-15-3594-9

[8] Z. Er-reguig and H. Ammor, "Towards designing a microcell base station using a software-defined radio platform," in *Proc. 7th Medit. Congr. Telecommun. (CMT)*, Oct. 2019, pp. 1–4.

[9] K. Haneda, E. Kahra, S. Wyne, C. Icheln, and P. Vainikainen, "Measurement of loop-back interference channels for outdoor-to-indoor full-duplex radio relays," in *Proc. 4th Eur. Conf. Antennas Propag. (EuCAP)*, Barcelona, Spain, Apr. 2010, pp. 1–5.

[10] J. M. Rigelsford, K. L. Ford, and L. Subrt, "A passive system for increasing cellular coverage within energy efficient buildings," in *Proc. 8th Eur. Conf. Antennas Propag. (EuCAP)*, Apr. 2014, pp. 614–615.

[11] K. Ntontin and C. Verikoukis, "Relay-aided outdoor-to-indoor communication in millimeter-wave cellular networks," *IEEE Syst. J.*, vol. 14, no. 2, pp. 2473–2484, Jun. 2020.

[12] A. Asp, A. Baniya, S. F. Yunas, J. Niemelae, and M. Valkama, "Applicability of frequency selective surfaces to enhance mobile network coverage in future energy-efficient built environments," in *Proc. 21st Eur. Wireless*, May 2015, pp. 1–8.

[13] L. W. Doors. *Signal Window*. Accessed: Feb. 13, 2023. [Online]. Available: http://signal-window.com/

[14] J. Lilja, "Mobile-friendly glass—Comparing solutions from the end user viewpoint," in *Proc. Glass Perform. Days*, Tampere, Finland, Jun. 2019, pp. 1–4.

[15] L. Vähä-Savo et al., "Passive antenna systems embedded into a load bearing wall for improved radio transparency," in *Proc. 50th Eur. Microw. Conf. (EuMC)*, Jan. 2021, pp. 424–427.

[16] Ministry of the Environment of Finland. (Dec. 2017). *1010/2017 Decree of the Ministry of the Environment on the Energy Performance of New Buildings*. [Online]. Available: https://ym.fi/en/the-national-building-code-of-finland

[17] Recommendation ITU-R P.2040-2. (Sep. 2021). *Effects of Building Materials and Structures on Radiowave Propagation Above About 100 MHz*. [Online]. Available: https://www.itu.int/dms_pubrec/itu-r/rec/p/R-REC-P.2040-2-202109-I!!PDF-E.pdf

[18] S. Tretyakov, *Analytical Modeling in Applied Electromagnetics*. Norwood, MA, USA: Artech House, 2003.

[19] *Building Components and Building Elements—Thermal Resistance and Thermal Transmittance—Calculation Methods*, Standard ISO 6946:2017, Dec. 2021.

[20] *Building Materials and Products—Hygrothermal Properties—Tabulated Design Values and Procedures for Determining Declared and Design Thermal Values*, Standard ISO 10456:2007, Dec. 2017.

[21] L. Vähä-Savo, K. Haneda, C. Icheln, and X. Lü, "3D model of antenna system embedded into building envelope for improved cellular signal transmission through load-bearing walls," Dept. Electron. Nanoeng., Aalto Univ. School Elect. Eng., Espoo, Feb. 2023, doi: 10.5281/zenodo.7615114.

[22] K. Vinayagamoorthy, J. Coetzee, and D. Jayalath, "Microstrip to parallel strip balun as spiral antenna feed," in *Proc. IEEE 75th Veh. Technol. Conf. (VTC Spring)*, May 2012, pp. 1–5.

[23] *Building Code Requirements for Structural Concrete: An ACI Standard; Commentary on Building Code Requirements for Structural Concrete*, Standard ACI 318-19, American Concrete Institute, 2019.

[24] L. Veggi, L. Vähä-Savo, K. Haneda, E. M. Vitucci, and V. Degli-Esposti, "Electromagnetic and thermal analysis of coaxial cable connection embedded in an intelligent wall," in *Proc. 17th Eur. Conf. Antennas Propag. (EuCAP)*, Florence, Italy, Mar. 2023, pp. 1–4.

Lauri Vähä-Savo (Graduate Student Member, IEEE) received the B.E. and M.E. degrees from the Aalto University School of Electrical Engineering, Espoo, Finland, in 2016 and 2019, respectively. He is currently pursuing the D.Sc. degree with the Department of Electronics and Nanosciences within the Antennas and Propagation Group, Aalto University, Espoo.

He is currently working in the field of 5G antennas and outdoor-to-indoor communication. His research interests include a microwave and millimeter-wave antenna design, human antenna interaction, and smart buildings and cities.

Katsuyuki Haneda (Member, IEEE) is currently an Associate Professor with the Aalto University School of Electrical Engineering, Espoo, Finland. He has author and coauthor of several best paper and student paper awards in the IEEE Vehicular Technology Conference and European Conference on Antennas and Propagation, among others. His current research interests include high-frequency radios such as millimeter-wave and beyond and wireless for medical and smart-city applications.

Prof. Haneda received the R.W.P. King paper award of the IEEE TRANSACTIONS ON ANTENNAS AND PROPAGATION in 2021, together with Dr. Usman Virk. He was an Associate Editor of the IEEE TRANSACTIONS ON ANTENNAS AND PROPAGATION between 2012 and 2016, and an Editor of the IEEE TRANSACTIONS ON WIRELESS COMMUNICATIONS between 2013 and 2018. He was a Guest Editor of Special Issues on Antennas and Propagation Aspects of In-Band Full-Duplex Applications and on Artificial Intelligence in Radio Propagation for Communications in IEEE TRANSACTIONS ON ANTENNAS AND PROPAGATION in 2021 and 2022, respectively. He is also a Guest Editor of the forthcoming Special Section on Sub-THz and THz Radio Propagation: Measurements and Characterization in the IEEE OPEN JOURNAL OF ANTENNAS AND PROPAGATION. He was a Co-Chair of a disciplinary working group on radio channels in European COST Actions CA15104 Inclusive Radio Communication Networks for 5G and beyond (IRACON) between 2016 and 2020. He is a Technical Programme Committee Co-Chair of the 17th European Conference on Antennas and Propagation (EuCAP 2023), Florence, Italy.

Clemens Icheln received the Dipl.Ing. degree in electrical engineering from the Harburg University of Technology, Hamburg, Germany, in 1996, and the Licentiate and the D.Sc.Tech. degrees in radio engineering from Aalto University, Espoo, Finland, in 1999 and 2001, respectively.

He is currently a University Lecturer with the Department of Electronics and Nanoengineering, Aalto University School of Electrical Engineering, Espoo. His current research interests include the design of multi-element antennas for small communication devices such as mobile terminals and medical implants, to operate at frequency ranges as low as 400 MHz but also up to mm-wave frequencies, as well as the development of suitable antenna characterization methods that allow taking, e.g., the effects of the radio channel into account.

Xiaoshu Lü leads the team of Renewable Energy and Low Carbon Buildings with the University of Vaasa, Vaasa, Finland, and holds an Adjunct Professorship in Artificial Intelligence and Big Data Applications to Buildings at Aalto University, Espoo, Finland. Her research interests include energy-efficient buildings and indoor environmental quality, energy efficiency technologies for renewable and unconventional energy resources, as well as hybrid energy systems for low-carbon buildings. Her research primarily focuses on developing numerical evaluation methods to accurately assess the thermal insulation properties of building walls. She is extensively involved in researching how hybrid renewable and storage energy systems with control strategies can address the challenges of intermittent renewables to decarbonizing built environment at building, district, and urban scales. Additionally, she maintains a keen interest in examining the impact of various wireless services on the energy performance of energy-efficient buildings. She actively explores the integration of passive antenna systems embedded into building walls as a viable solution for enhancing indoor coverage.